

Optimization of Flame Synthesis for Carbon Nanotubes Using Supported Catalyst

Randall L. Vander Wal,* Lee J. Hall, and Gordon M. Berger

The National Center for Microgravity Research (NCMR), c/o The NASA-Glenn Research Center,
M.S. 110-3, 21000 Brookpark Road, Cleveland, Ohio 44135

Received: March 4, 2002; In Final Form: September 4, 2002

A series of rich premixed flames are used to realize a post-flame gas mixture for optimum carbon nanotube (CNT) growth using inexpensive hydrocarbon fuels. The mixture of CO, CO₂, H₂, and H₂O is varied through use of hydrocarbon fuels with different H/C ratio in flames with different fuel/air ratios. Both SEM and HRTEM imaging are used to correlate the nanotube morphology and internal structure to the reaction gas composition. The variations observed are understood in light of the gas composition and the interaction of the reactive components with both the deposited Co catalyst particles and supporting metal substrate. Further comparisons between flames producing the same CO or H₂ concentrations identify the roles of these gases in CNT synthesis. Optimal flame synthesis conditions, defined upon a H₂ and CO concentration map, are gauged on the basis of CNT length, relative surface density, and level of graphitic structure.

Introduction

Carbon nanotubes are widely sought for a wide variety of applications including gas storage,¹ absorption,² intercalation media,^{3–5} catalyst support,^{6–8} and composite reinforcing material.^{9–12} Each of these applications, however, may require redispersal of the collected CNTs and attachment to a support structure. CVD methods are favored for CNT synthesis,^{13–21} despite subsequent harvesting and purification issues.^{22–24} If the CNTs could be synthesized directly upon the support to be used in the end application, a tremendous savings in postsynthesis processing could be realized. A second consideration is that these applications will require large scale production to generate commercial interest. Current CVD methods are ill-equipped to achieve this goal. Constrained by the confines of an electrically heated furnace, these methods are energy intensive, geometrically confined, and not scalable.

We have pursued flame synthesis as an economical method for bulk synthesis of single-walled nanotubes (SWNTs) and carbon nanofibers using both aerosol catalysts^{25–31} and supported catalysts.^{32,33} Related work has appeared recently.^{34,35} Flame systems are used in industry for large scale energy production, drying, and material processing.³⁶ With respect to CNT synthesis, a flame can be energy efficient where a portion of the fuel gas is burnt to produce the elevated temperature while the remainder serves as the growth reagent. Moreover, flame systems are geometrically versatile, as illustrated by innumerable boiler and furnace designs.³⁷

Compared to diffusion flames, premixed flames offer several advantages for CNT synthesis which include the following:

1. A wide selection of fuels.
2. Ability to adjust the stoichiometry of the reaction gases yielding different flame chemical compositions.
3. Additional freedom to adjust the flame temperature, apart from the stoichiometry.
4. Scalability—Premixed flames are not limited by diffusion; the reactive gas profile can be made uniform by the burner system.

5. Ability for continuous, multi-staged processing.

With these advantages providing motivation, we explored the utility of a premixed flame for CNT synthesis using supported catalysts upon stainless steel mesh. Our fuel selection of inexpensive, commercial hydrocarbon fuels was guided by the motivation of economic scalability. Natural gas or its component gases such as ethane, propane, and even ethylene satisfy this criterion. In this paper the capability to vary the reactive gas composition is exercised to map a reactive gas mixture region conducive to CNT synthesis using these fuels. The results are interpreted through the interaction between the post-flame gases, the supported catalyst, and underlying metal support. Scanning electron microscopy (SEM) and high-resolution transmission electron microscopy (HRTEM) are used to map the morphology and nanostructure of the CNTs, respectively. Presented here is the first report correlating a flame's chemical composition to CNT morphological structure, graphitic quality, and relative yield as observed via SEM and HRTEM.

Experimental

Premixed flames were supported on a water-cooled, sintered metal burner. The burner diameter was 50 mm surrounded by a 5 mm annular ring, also of sintered metal, providing an inert shield gas flow. A conical chimney with a 45 degree taper, whose base matched the burner diameter, fed a 1 in. O.D. stainless steel tube 1.5 in. long. Chimneys made from straight sections of stainless steel tube also proved viable. At the top of the chimney, a circular molybdenum ring held the mesh-supported catalyst within the post-flame gases. The flame equivalence ratio was varied, adjusting the fuel flow rate to the burner while maintaining the air flow at 11.5 SLP. The fuels were supplied by Matheson as CP grade, while acetylene was 96% acetylene dissolved in acetone.

The post-flame gas temperature, measured using a type K thermocouple, was 800 °C. No radiation correction was applied, as the mesh within the flame would suffer similar losses while the radiation correction was within estimated measurement uncertainty, ± 25 °C.³⁸ The flame gas composition was calculated with a chemical equilibrium code on the basis of the

* Corresponding author. Ph.: (216) 433-9065. Fax: (216) 433-3793.
E-mail: randy@rvander.grc.nasa.gov.

TABLE 1: Post-flame Gas Composition of a Range of Fuel/Air Flames Calculated To Determine Feasibility of Growth for Carbon Nanotubes

fuel	fuel/air equivalence ratio (ϕ)	mole fraction H ₂	mole fraction CO	mole fraction H ₂ O	mole fraction CO ₂
CH ₄	1.47	0.104	0.0524	0.142	0.0707
	1.62	0.133	0.0668	0.128	0.0640
	2.00	0.197	0.0988	0.0988	0.0492
C ₂ H ₆	1.52	0.105	0.0699	0.115	0.0763
	1.62	0.122	0.0817	0.106	0.0706
	1.83	0.157	0.105	0.0897	0.0595
C ₃ H ₈	1.50	0.0965	0.0726	0.108	0.0806
	1.62	0.117	0.0882	0.0977	0.0730
	1.74	0.137	0.103	0.0880	0.0657
C ₂ H ₄	1.81	0.146	0.110	0.0834	0.0623
	1.87	0.155	0.117	0.0790	0.0589
	1.37	0.0661	0.0664	0.0974	0.0971
C ₂ H ₂	1.50	0.0859	0.0862	0.0873	0.0870
	1.62	0.104	0.105	0.0779	0.0776
	1.74	0.122	0.122	0.0690	0.0686
C ₂ H ₂	1.81	0.131	0.131	0.0647	0.0644
	1.43	0.0522	0.105	0.0522	0.104
	1.50	0.0593	0.119	0.0484	0.0964
C ₂ H ₂	1.62	0.0722	0.145	0.0413	0.0823

measured post-flame temperature, initial fuel identity, and the fuel–air equivalence ratio as inputs.³⁹ Table 1 lists the fuels and fuel/air equivalence ratios (ϕ = the experimental fuel/air ratio divided by the stoichiometric fuel/air ratio) for the flames studied here and the corresponding equilibrium gas compositions.

Type 304 stainless steel (SS) meshes (400 \times 400 mesh with 0.0009 in. diameter wire) were coated with cobalt as catalyst. A submonolayer film (<10 nm) of cobalt was applied to the meshes by physical vapor deposition (PVD). In this manner, metal islands resembling droplets were formed upon the mesh support to serve as catalyst particles. All meshes used in the present studies were prepared in the same manner. Meshes were retained in the flame gases for 12 min, measured from the time of insertion to extraction. Samples were collected from the flame and cooled by immersion in flowing N₂ through a 1 in. diameter quartz tube. This cooled the sample within a minute to avoid air oxidation.

SEM images were obtained using a Hitachi S4700 instrument with a tungsten single-crystal cold field emission electron source operated at 6 kV. Images were collected using a mixed detector mode with upper and lower secondary electron detectors. TEM images were taken using a Phillips CM200 with Gatan image filter (GIF) for digital imaging with live Fourier transforms. The instrument operated at 200 kV using a LaB₆ filament.

Results

Within a premixed flame, the fuel and oxidizer are thoroughly mixed prior to combustion. Complete fuel breakdown occurs prior to product formation. Therein, we interpret our results on the basis of the post-flame gas compositions. Upon testing different hydrocarbon fuels and equivalence ratios, a common theme that emerged was the relation between the CO and H₂ concentrations and the CNT synthesis results. Direct use of CO or H₂ brings attendant concerns of high toxicity or extreme flammability, so fell outside our practical fuel set. For stoichiometries not near the rich flammability limit or the soot inception equivalence ratio, the products will consist of a mixture of CO, H₂, CO₂, and H₂O.^{37,39} Using a simple hydrocarbon fuel dictates the ratio of CO/H₂ and CO₂/H₂O through the fuel molecular formula and the fuel/air equivalence ratio.^{37,39} By

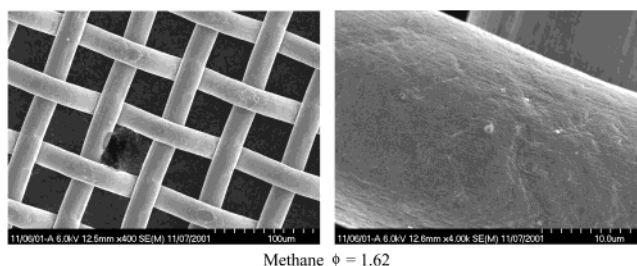


Figure 1. A series of SEM images of the catalyst-coated SS mesh immersed within the methane flame gases at $\phi = 1.62$. The complete absence of CNT synthesis is evident. The scale is indicated by the lower right-hand ruler. All tested methane flame conditions produced similar results.

increasing the fuel/oxidizer ratio beyond stoichiometric, combustion becomes less complete; the CO and H₂ concentrations increase while those of CO₂ and H₂O correspondingly decrease.

To study the effects of different CO and H₂ concentrations upon CNT synthesis, various fuel/air equivalence ratios and different hydrocarbon fuels (possessing different C/H ratios) were tested. To facilitate subsequent comparisons, several fuel/air stoichiometries (using different fuels) were chosen to maintain either the same CO or H₂ mole fraction within the combustion products. Table 1 lists the post-flame gas compositions, organized by fuel identity and equivalence ratio studied. Lower ϕ values than those tabulated produced far less, if any, CNT growth (CH₄, C₂H₆, C₃H₈, C₂H₄) while higher ϕ values yielded unstable flames (CH₄, C₂H₆, C₃H₈) or soot (C₂H₄, C₂H₂), as witnessed by visible yellow emission from the flame. It should be noted that all listed conditions correspond to fuel-rich conditions, producing CO and H₂ in the post-flame gases as incomplete combustion products. Temperatures were measured to be rather invariant with respect to fuel and flame conditions, despite variations in the adiabatic flame temperature. Higher enthalpy flames with higher burning velocities will experience higher heat losses to the burner. Other aspects of the experimental geometry such as the sample position of roughly 8 cm downstream from the flame front, mounted in a holder within a chimney, further minimized sample temperature variations. These factors brought possible variations of post-flame temperature to within the measurement uncertainty. Consequently the value of 800 °C was used for the equilibrium chemical calculations to calculate the post-flame gas composition.

Located well-downstream from the flame, radical concentrations such as OH are negligible at temperatures less than 1000 °C, (<10⁻⁴ mole fraction).^{37,39} More detailed chemical computational codes confirm that for the range of equivalence ratios and fuels used here, the concentrations of other fuel pyrolysis products such as C₂H₂ (and hence other species derived from it, such as PAHs) may be considered negligible. Therefore, CO and H₂ are regarded as the active contributors to CNT synthesis, mediating both carbon deposition and surface catalytic activity. Hence, we interpret our results in terms of the concentrations of these constituents. We note that even within this regime, there are significant concentrations of H₂O and CO₂. However, these gases are of secondary consideration in CNT synthesis and their roles are discussed later.

SEM Comparisons. Methane. In the context of our experimental conditions with ϕ ranging from 1.47 to 2.00, methane (CH₄) was inactive toward CNT synthesis as illustrated in Figure 1.

Ethane. Ethane (C₂H₆) was the first hydrocarbon fuel tested that was viable for CNT synthesis. Figure 2 illustrates the range

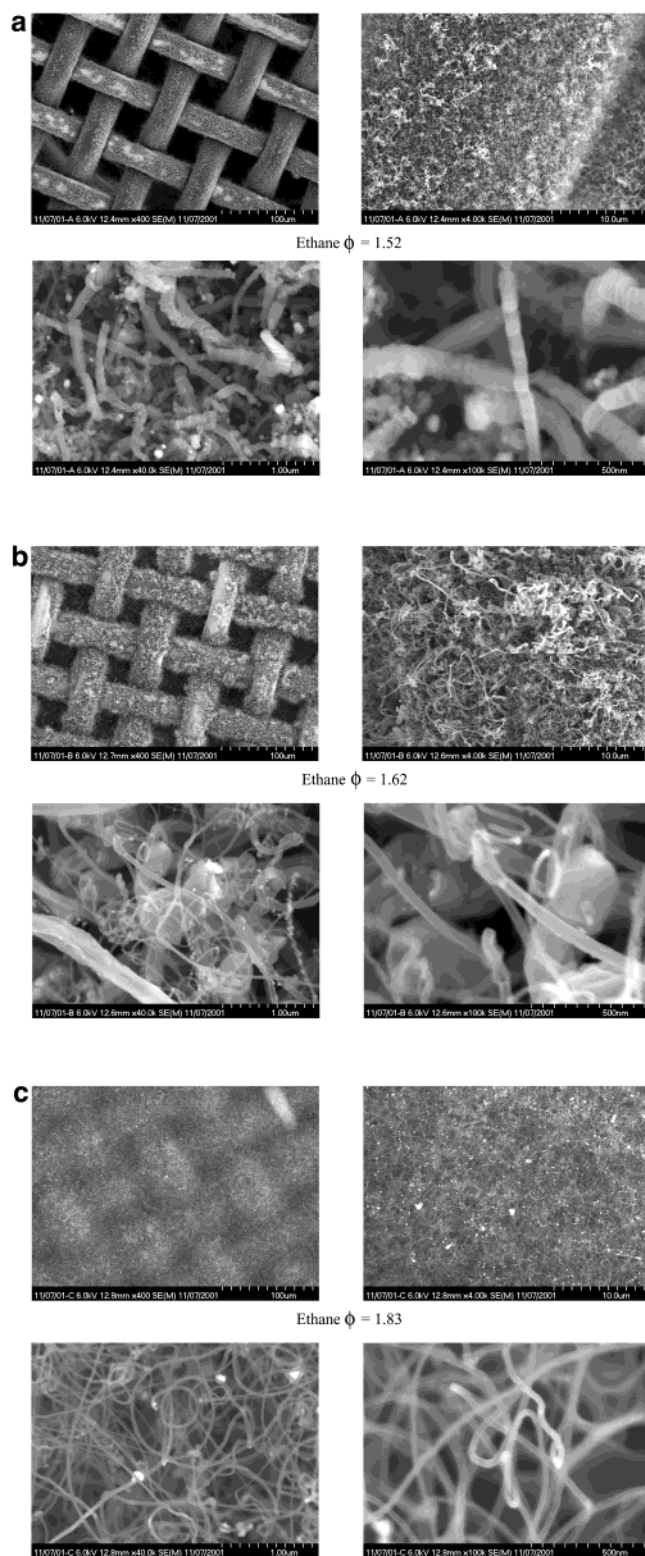


Figure 2. A series of SEM images for the catalyst-coated SS mesh immersed within the flame gases produced by an ethane flame at (a) $\phi = 1.52$, (b) $\phi = 1.62$, and (c) $\phi = 1.83$. Particles are evident at many tips of the catalyzed products, many of which appear to be nanofibers, not CNTs as seen in (a). The surface coverage is improved in (b) but a variety of products are evident. The best growth density and uniformity of product (CNTs) is seen in (c).

of carbon nanofilaments produced by the different post-flame gas compositions established by the fuel/air ratios for C_2H_6 . The lowest ϕ , 1.52 (Figure 2a), results in patchy surface coverage, and a wide variety of catalyzed products, ranging from nanofi-

bers to CNTs. Short, large-diameter nanofibers appear to be the dominant product. Their segmented structure and irregular geometry suggest a high level of defects or misalignments within the nanofiber. Catalyst particles, which appear as bright spots due to greater electron scattering intensity at the SEM detector, are also evident at some tips of the nanofibers. A variety of stubby and slender nanofibers was produced for $\phi = 1.62$ (Figure 2b). The best relative yield and quality as discerned from the SEM overview of morphology and uniformity seen in Figure 2c was obtained using $\phi = 1.83$. As suggested by the contrast variation in the high magnification image, many of the nanofilaments appear to be hollow CNTs. A characteristic of CNTs with large hollow cores is a corresponding high degree of graphitic quality, as will be shown in corresponding TEM images.

Ethylene. The results observed for ethylene (C_2H_4) are shown in Figure 3. Flames produced by C_2H_4 at $\phi = 1.50$ support CNT growth, but only barely, as seen in Figure 3a. The surface coverage is sparse and, though some CNTs are formed, additional stubs and clumps of carbon are produced. The best results have been observed, as reported elsewhere, using $\phi = 1.62$ (Figure 3b).³² As Figure 3b shows, the CNTs are gently curved, without bends or twists. MWNTs are confirmed by the TEM images (shown later in Figure 7), which reveal a highly uniform tubular structure. Moreover, as seen in the SEM image, the CNTs exhibit a high degree of uniformity of size and nanostructure. High ϕ values for C_2H_4 (e.g., 1.8, Figure 3c) produce a gas environment less conducive to CNT growth. A significantly wider distribution in diameter and a greater variation in morphology is observed; far fewer CNTs are found. The observed structures are highly contorted, segmented, solid units. Catalyst particles are evident at some exposed sections of these growths, as with C_2H_6 at $\phi = 1.52$.

Acetylene. Similar observations apply to each of the acetylene (C_2H_2) cases, as displayed by Figure 4. As illustrated, a variety of catalyzed structures, ranging from nanofibers to nanotubes, are evident under each flame condition. In all cases, the density of growth is high, unlike for the ethane and ethylene flames. Notably, the morphology, relative density, and internal structure (as will be further illustrated by TEM images) is vastly different between the C_2H_2 flame at $\phi = 1.62$ and the corresponding C_2H_4 and C_2H_6 cases at $\phi = 1.62$. This clearly shows the flame equivalence ratio is not the determining factor in generating favorable CNT synthesis conditions.

Propane. Results for the propane (C_3H_8) samples as revealed by SEM and TEM images were judged to be rather similar to those for either C_2H_6 or C_2H_4 flames for equivalence ratios producing identical CO or H_2 concentrations. Consequently, these results will not be discussed further, but are implicit in the discussion for the other flame systems.

While the H_2/CO ratio produces significant variations in the types of catalyzed products, it also does not strictly govern synthesis conditions. This may be observed by comparing the results for any particular fuel at the different ϕ values studied. This is further illustrated by comparing the SEM images for C_2H_6 at $\phi = 1.83$ (Figure 2c) with those for C_2H_4 at $\phi = 1.62$ (Figure 3b) and C_2H_2 at $\phi = 1.50$ (Figure 4b). Each of these flame conditions produced the best results for CNT synthesis with its particular fuel; the results are self-evident. Clearly, the concentrations of the individual post-flame gases, particularly CO and H_2 , are the relevant variables.

CNT Synthesis Region: CO and H_2 Concentrations. Figure 5 plots the CO and H_2 concentrations for the different

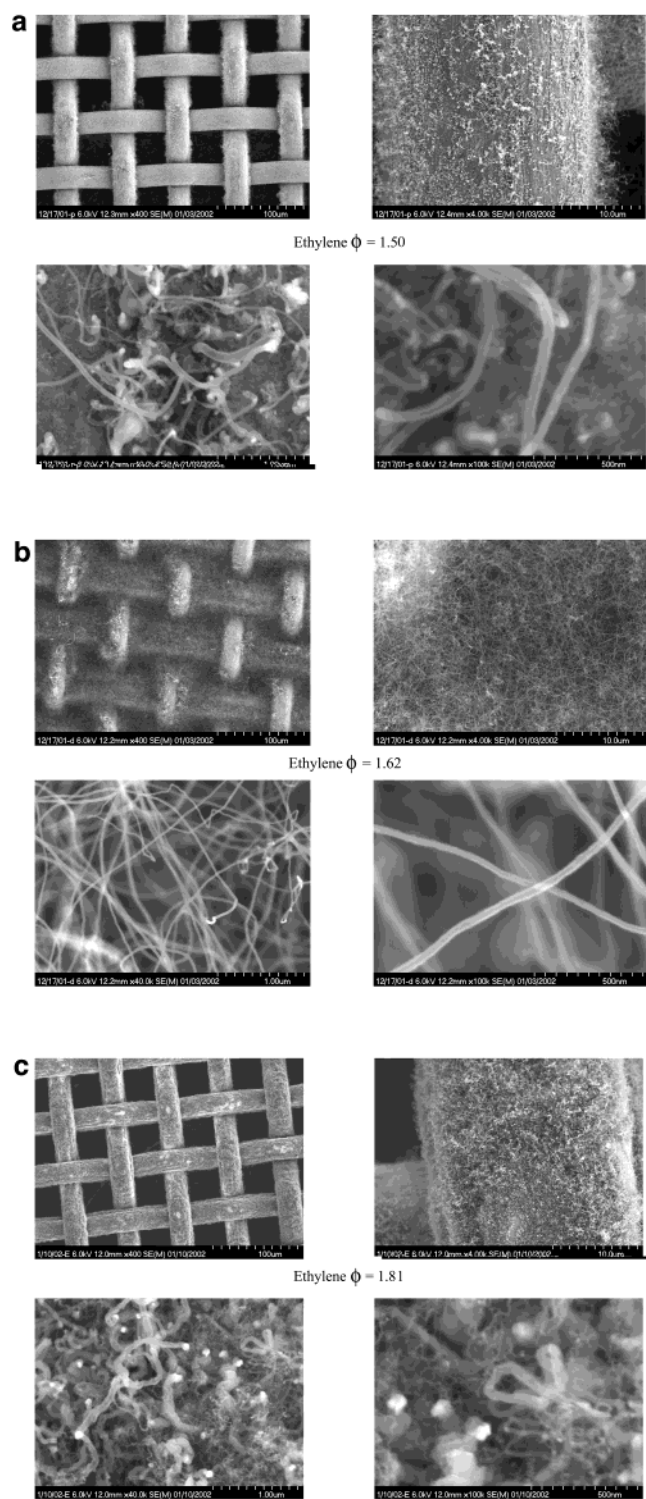


Figure 3. A series of SEM images for the catalyst-coated SS mesh immersed within the flame gases produced by an ethylene flame at (a) $\phi = 1.50$, (b) $\phi = 1.62$, and (c) $\phi = 1.81$. A very low growth density is produced using flame conditions in (a). An optimum growth density and CNT uniformity is produced using a fuel–air equivalence ratio of $\phi = 1.62$, condition (b). The highest ϕ , 1.81, leads to a significantly lower yield in addition to heterogeneity of products along with catalyst particles detached from the surface.

fuels over the range of equivalence ratios investigated in the present work. Each fuel–air equivalence ratio presents a unique H_2/CO ratio providing a range of concentrations between these two post-flame products. Each line segment represents the CO and H_2 product concentration range for each fuel, dependent

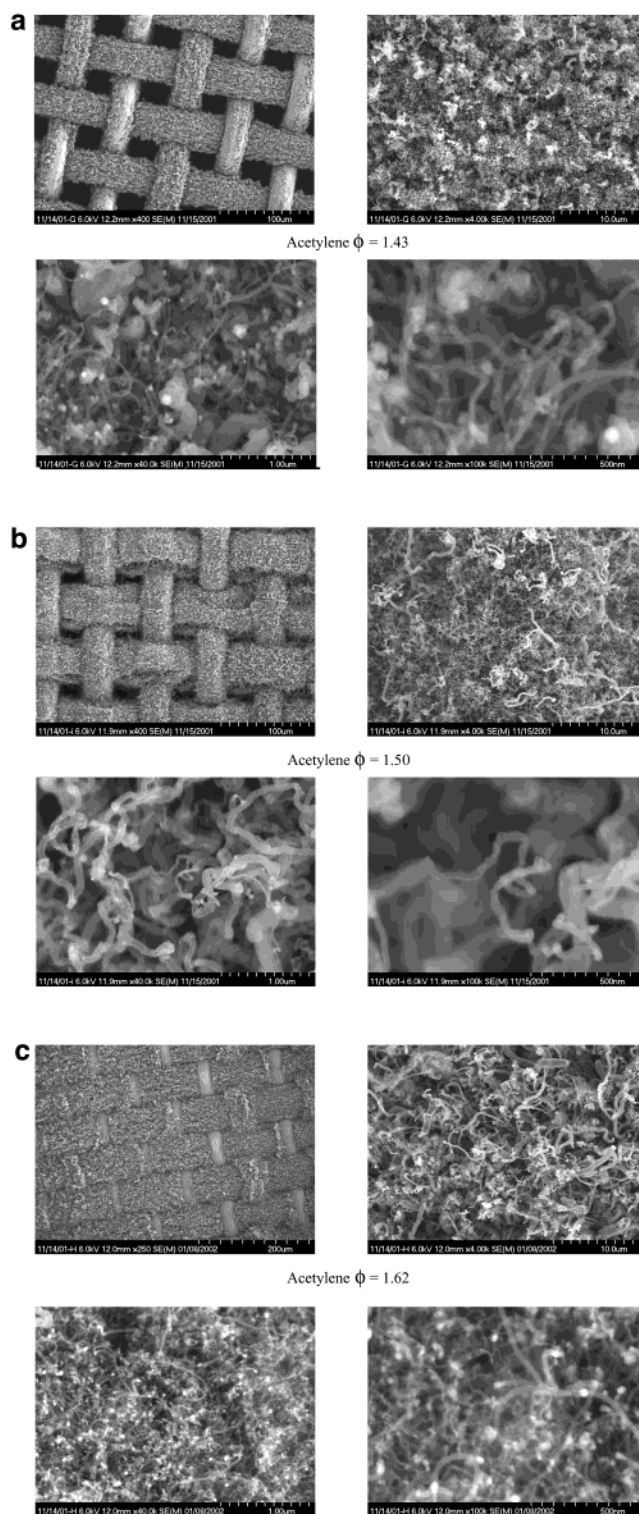


Figure 4. A series of SEM images for the catalyst-coated SS mesh immersed within the flame gases produced by an acetylene flame at (a) $\phi = 1.43$, (b) $\phi = 1.50$, and (c) $\phi = 1.62$. Despite the high density of catalyzed products, a vast array of products, few of which are CNTs, is produced by the lowest ϕ of 1.43 (a). While increasing ϕ leads to increased surface coverage, the morphology of the catalyzed products also increases in variety. Catalyst particles, detached from the surface, are evident at many nanofiber tips. The best uniformity appears to be that produced by the flame conditions in (b).

on the fuel/air equivalence ratio.³⁹ The shaded region in the figure represents the range of combined CO and H_2 concentrations from various fuels conducive to CNT catalysis, as judged by SEM and TEM images presented subsequently.

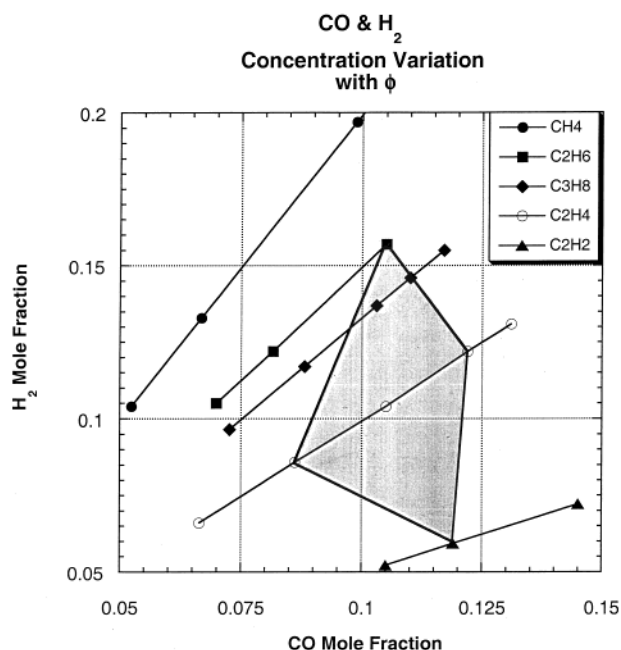


Figure 5. A mole fraction concentration map of CO and H₂ produced by burning the indicated fuels at various equivalence ratios in a premixed flame configuration. The shaded region demarcates the region of H₂ and CO concentrations judged suitable for CNT synthesis on the basis of SEM and TEM images.

It should be understood that the boundaries of this region are somewhat subjective and are only approximate, given the limited number of data points to define this region. Not all combinations of CO and H₂ concentrations are equally viable, nor necessarily desirable, given variations in the relative yield and quality of the catalyzed products. The end application will ultimately determine these tolerances. For our purposes, we did not exclude conditions based on these factors but merely whether CNTs were synthesized.

The utility of the plot shown in Figure 5 is that it provides ready insight into suitable gas-phase compositions for CNT synthesis determined by the flame product compositions. These quantities are readily derived from the fuel–air equivalence ratio using chemical equilibria code and may be further adjusted by post-flame gas addition. To illustrate these concepts, SEM images and TEM images will be shown to correlate the flame conditions with the catalyzed products.

As the SEM and TEM images will show, different H₂/CO ratios are active toward CNT synthesis. However, for any given ratio, there appears to be only a narrow range of concentrations of each gas that result in high yield of graphitic CNTs. By proper selection of the flame equivalence ratio, direct comparison is made between flames where only the CO or H₂ concentration was varied.

Over the concentration range indicated by the shaded region, there is a strong interplay between the gas-phase composition, the deposited catalyst particles, and the support surface. While the deposited Co catalyst particle is more active for reasons based on geometry and surface area, the underlying SS support can also directly participate in CNT and nanofiber catalysis. The relative contributions of these different catalyst systems to the observed CNT growth is reflected in the CNT growth density upon the mesh, uniformity, and graphitic quality. SEM is used to assess the yield as the relative surface coverage of the mesh with CNTs. TEM is used to assess the graphitic quality of the nanotubes.

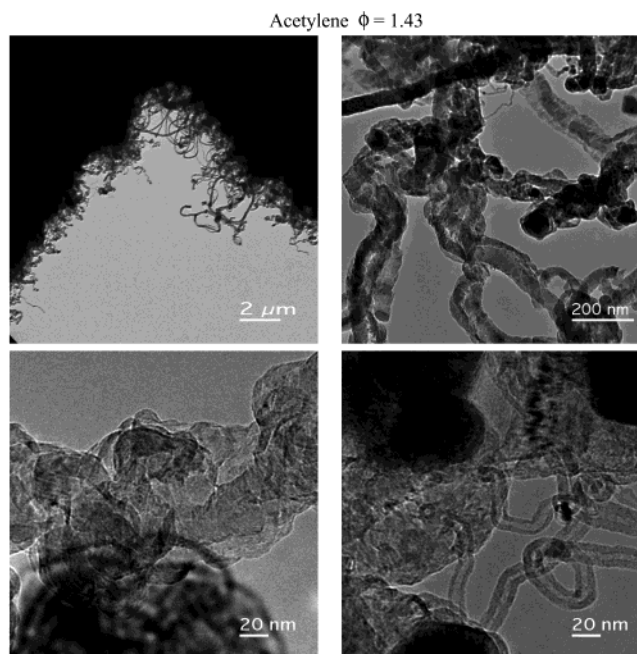


Figure 6. A series of TEM images for the catalyst-coated SS mesh immersed within the flame gases produced by an acetylene flame at $\phi = 1.43$. The nonuniformity and variety of catalyzed products ranging from CNTs to solid nanofibers is evident from the images.

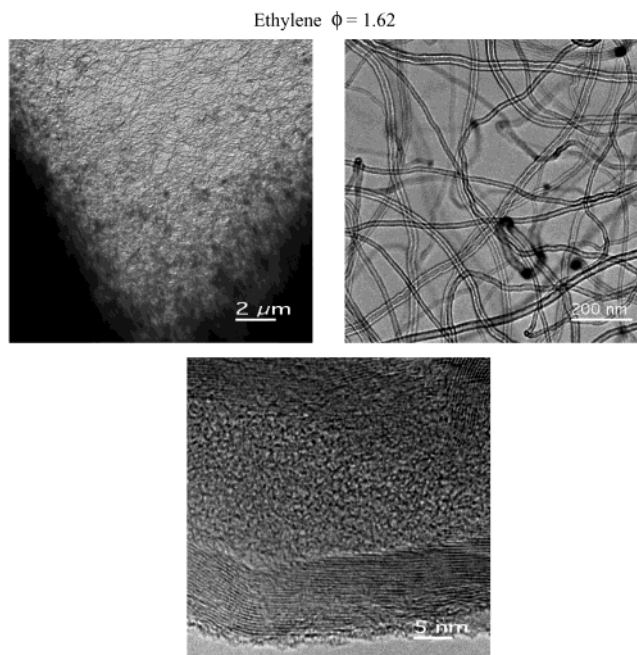


Figure 7. A series of TEM images for the catalyst-coated SS mesh immersed within the flame gases produced by an ethylene flame at $\phi = 1.62$. A high density of graphitic CNTs of uniform diameter is evident from the images, consistent with the SEM images.

H₂ and CO Concentrations: TEM Comparisons. If comparisons are made between the C₂H₂ flame at $\phi = 1.43$ (Figure 6a), the C₂H₄ flame at $\phi = 1.62$ (Figure 7b), and the C₂H₆ flame at $\phi = 1.83$ (Figure 8c), results from flames with equal post-flame CO mole fractions may be contrasted. The images were taken directly from the mesh treated within the flame, without any subsequent purification or processing. With increasing H₂ concentration at a CO mole fraction of 0.105, significant quantities of CNTs are produced. Their diameter decreases, length increases, and the level of long-range graphitic structure increases between the C₂H₂ flame with $\phi = 1.43$ and

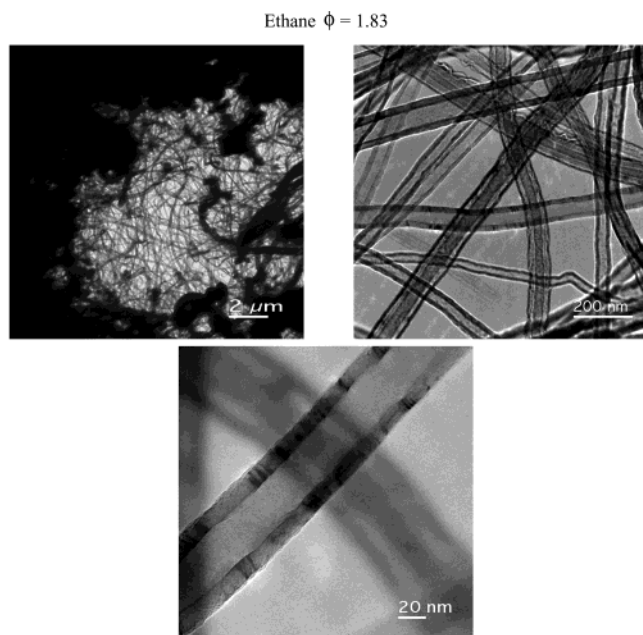


Figure 8. A series of TEM images for the catalyst-coated SS mesh immersed within the flame gases produced by an ethane flame at $\phi = 1.83$. Though graphitic CNTs are produced, a wider variety of catalyzed products is evident in the lower-magnification images.

the C_2H_4 flame with $\phi = 1.62$ as shown in the corresponding TEM images of Figures 6 and 7, respectively. Concurrently, the relative yield of nanofibers and contorted solid forms decreases. However, this trend does not continue. As the H_2 mole fraction rises, the yield and quality of the CNTs remains similar, but their size changes. Even though the SEM images between the C_2H_4 and C_2H_6 cases appear to possess similar CNT surface densities, as the TEM images of the C_2H_4 and C_2H_6 flames show (Figures 7 and 8, respectively), the catalyzed CNTs are quite different. Those produced from C_2H_6 , though highly graphitic, are significantly larger, yet the CNTs are still rather uniform in diameter.

As the concentration of the carbon-containing gas is of prime importance in CNT synthesis, we further explore the effects of reactant mole fractions by illustrating the effect of post-flame CO concentration for a fixed H_2 concentration within the CNT synthesis region. Figure 9 shows TEM images of CNTs, as produced at the lowest ϕ for C_2H_6 , 1.52. As observed in the low magnification image, a wide variety of structures are catalyzed. Tubular structures, characteristic of CNTs, were generally not observed. As the higher magnification image shows, the nanostructures that do form appear solid, contorted, and nongraphitic. An increased CO concentration, as realized using an C_2H_4 premixed flame of $\phi = 1.62$, yields a dramatic improvement in CNT yield and quality, as illustrated in Figure 7. With the same H_2 mole fraction as the C_2H_6 flame just examined, the higher CO mole fraction results in a vast yield increase of longer, thinner, and more uniform CNTs. Notably, there is a corresponding decrease in the undesirable types of non-CNT structures observed for C_2H_6 using $\phi = 1.52$ (Figure 9). The high-resolution image of a representative CNT reveals the high alignment of the graphitic layers, oriented parallel to the CNT axis. However, this trend in quantity and quality with increasing CO concentration does not continue. By using an C_2H_2 -fueled flame, a higher CO concentration may be realized while maintaining a similar H_2 concentration (higher ϕ values led to PAH and soot growth). As observed by comparing the SEM images of Figures 3 and 4, the C_2H_2 flame at $\phi = 1.62$

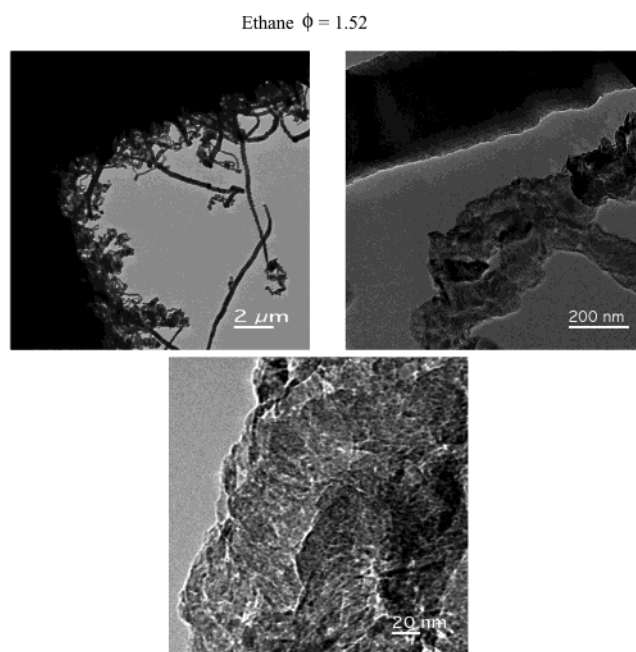


Figure 9. A series of TEM images for the catalyst-coated SS mesh immersed within the flame gases produced by an ethane flame at $\phi = 1.52$. The lower growth density, apparent absence of CNTs, and poorly structured solid nanofibers are evident.

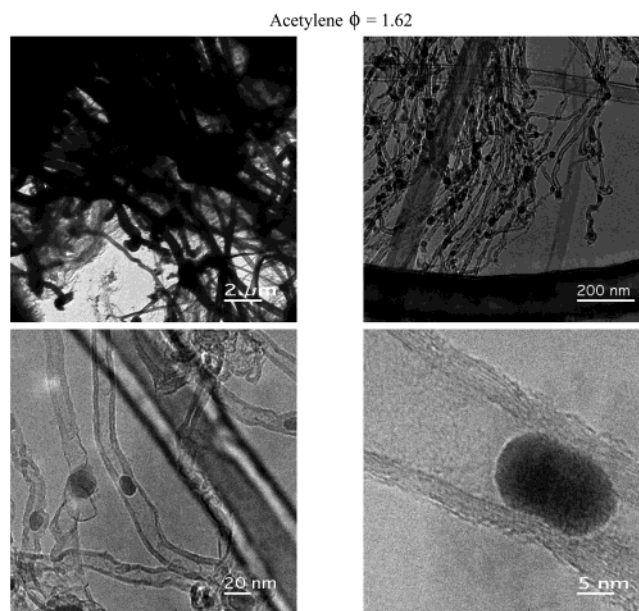


Figure 10. A series of TEM images for the catalyst-coated SS mesh immersed within the flame gases produced by an acetylene flame at $\phi = 1.62$. While solid nanofibers are catalyzed, many CNTs are also produced. Catalyst particles and their remnants are evident within many of the CNTs.

leads to the most dense CNT growth. This is confirmed by the TEM images of the mesh, as prepared in-situ, shown in Figure 10. Nanofilaments ranging from solid nanofibers to hollow CNTs are produced. This variability in morphology and size for both the CNTs and nanofibers is illustrated in the lower-magnification images of Figure 10. As observed in these images, many catalyst particles are now evident, both at the CNT tips and dispersed within the CNTs. Their heterogeneous size accounts for at least the diameters of particle-catalyzed CNTs. This observation stands in contrast to the general absence of either catalyst particles or fragments in the catalyzed products

in the C_2H_4 flame at $\phi = 1.62$ (Figure 7). Moreover, the degree of graphitic structure is now visibly poorer than for C_2H_4 at $\phi = 1.62$; many solid filaments are evident. These observations correlate with the corresponding SEM image for this flame (Figure 4c, showing the rich variety of catalyzed structures and catalyst particles detached from the substrate.

These results are understandable through (a) the interaction of the post-flame gases with the deposited catalyst particles and underlying metal support and (b) the effect of the individual gases on carbon deposition upon the particle surface and maintenance of its catalytic integrity. These topics are discussed next.

Discussion

Role of Catalyst Particle. Supported catalysts may form CNTs through either a base growth or a tip growth mechanism. In the former mode, the catalyst particle remains attached to the substrate while the CNT grows above the particle. In the latter mode, the catalyst particle leads the growth of the CNT and supplies carbon to the CNT behind itself.

Fundamental to either mode, hydrocarbons or CO undergo dissociative adsorption and the resulting carbon subsequently diffuses through and precipitates from the catalyst particle to add to the CNT. This has been well documented in the literature and is referred to here as the Carbon Solvation, Diffusion, Precipitation (CSDP) model.^{40–42} Inherent in this mechanism is that dissociative adsorption and carbon dissolution occur on different crystalline facets of the catalyst particle. It is possible that the underlying metal support can directly catalyze CNT growth or supply dissociative adsorption sites adjacent to the catalyst particle to source carbon to the CNT through the catalyst during base growth. In the latter scenario, the catalyst particle's crystalline structure would still govern the CNT size and morphology. As we subsequently demonstrate, the dominant growth mode depends on the post-flame gas composition as determined by ϕ .

With increasing CO concentration, as realized by an increased ϕ or alternative fuel, the rate of carbon deposition increases.^{43,44} Correspondingly, surface carbon builds to higher concentrations. If the dissolved carbon reaches a concentration sufficient to form a carbide phase, a second mode of CNT growth occurs. Now the resulting lattice mismatches between the carbide phase and underlying metal will create stresses localized within the surface region. Surface breakup will proceed along the weakest boundaries such as grain boundaries and edge dislocations where lattice stresses are concentrated and the carbon concentration will likely be highest. Uninhibited by surrounding metal and with the least contact surface area, the deposited catalyst particles are the most likely to detach from the surface. Surface asperities and other defect sites may also become detached from the surface to act as catalyst particles.

It is very arduous to directly examine surface breakup, as many of the CNTs will be firmly anchored to the catalyst particle which, in turn, are yet integral to the surface. Acid etching or oxidation processes to remove the CNTs from the surface will severely alter the surface structure and will introduce surface breakup by their application. This would completely obscure surface breakup due to partial carbide formation during the synthesis process. The postulate of surface breakup is based on the size and morphology variations observed in the catalyzed structures and is supported by dedicated studies investigating the evolution of catalyst “particles” through surface breakup processes.^{43,44,46,47}

Given the randomness of this breakup process, a wide variety of sizes and geometries would be expected for these nonideal

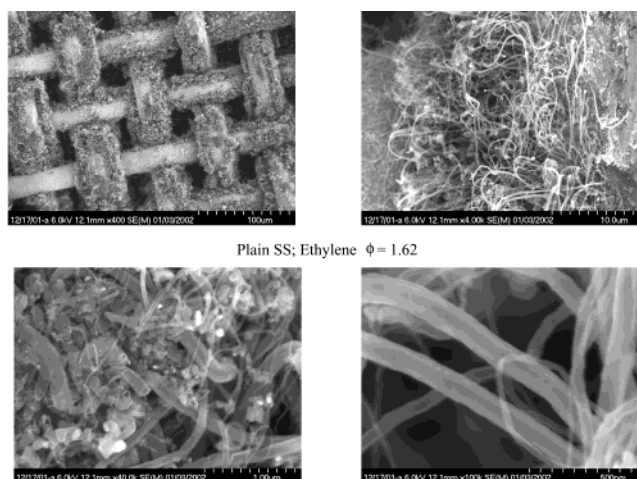


Figure 11. A series of SEM images for a plain (no catalyst deposit) SS mesh immersed within the flame gases produced by an ethylene flame at $\phi = 1.62$. While many CNTs are produced, neither their size nor surface coverage is uniform. The variety of diameters is evident in the highest magnification image. Catalyst particles, detached from the surface, are also evident within the images, indicative of surface breakup processes.

catalyst particles.^{45–51} A corresponding variability in the catalyzed carbon nanostructures would also be expected. Examples include the carbonaceous tufts, stubs, bushes, and other random carbon structures as evident in both the SEM and TEM images (Figures 4b and 10) for the C_2H_2 flame at $\phi = 1.62$.

Catalyst/Surface Interaction: Role of Steel Catalyst Support. The deposited catalyst particles provide not only a geometric enhancement by virtue of increased surface area and associated active sites for dissociative adsorption and carbon precipitation, but their uniformity of size lays the foundation for uniform CNT growth.

Ideally, the underlying SS mesh substrate serves only to support the catalyst particles. However, numerous studies related to coking phenomena have clearly demonstrated that steel and other alloys of transition metals can directly catalyze CNT and nanofiber growth.^{43–54} To address the relative contribution of the catalyst particles toward directing/controlling the CNT catalysis, a comparison was made between the uncoated SS mesh and SS mesh coated with Co catalyst. This comparison is also instructive for understanding the interaction of the flame gases with the deposited catalyst particles and underlying metal support.

SEM images of the uncoated SS mesh (Figure 11) may be compared with those shown in Figure 3b for the Co catalyst-coated mesh. Both meshes were treated using the ethylene flame with $\phi = 1.62$. The plain SS mesh is highly covered with carbonaceous growth. There is a noticeable lack of uniformity with regard to the mesh weave, i.e., cross wires are less densely covered. This has been characteristically observed in woven meshes and we attribute this difference to the mechanical stressing of the mesh cross wires during weaving. This “weaving stress” may facilitate surface catalysis by creating a strained surface that is relatively brittle through cold working the metal. This directional preference in growth density is one tell-tale sign of catalyst formation through surface breakup.

Another indicator of catalyst formation through surface breakup are the bright catalyst particles appearing at many CNT tips. Thus, in the absence of deposited catalyst particles, the CNTs and nanofibers appear to be formed through both base and tip growth. The higher-magnification SEM and TEM images

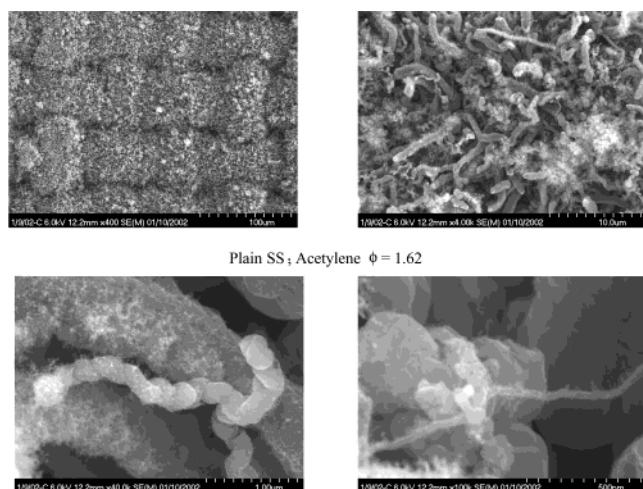
Plain SS; Acetylene $\phi = 1.62$

Figure 12. A series of SEM images for a plain (no catalyst deposit) SS mesh immersed within the flame gases produced by an acetylene flame at $\phi = 1.62$. A high yield of catalyzed products is produced. However, only nanofibers and other types of structures are synthesized.

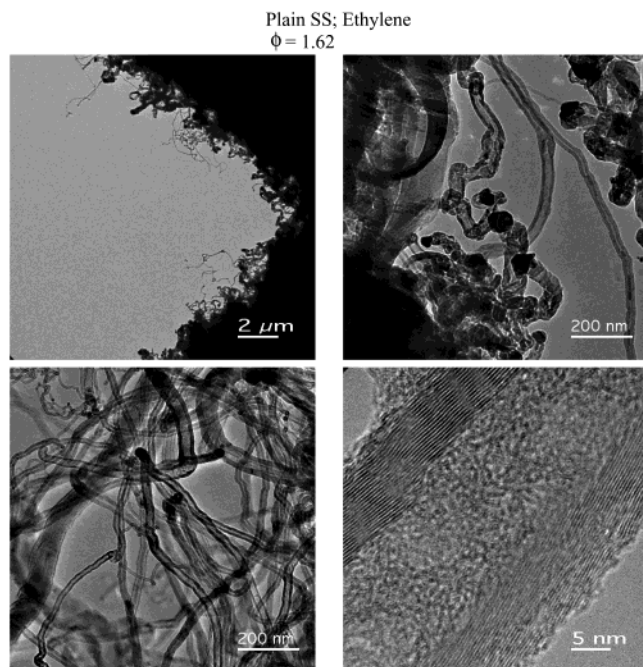
Plain SS; Ethylene
 $\phi = 1.62$

Figure 13. A series of TEM images for a plain (no catalyst deposit) SS mesh immersed within the flame gases produced by an ethylene flame at $\phi = 1.62$. The images illustrate the range of catalyzed products, such as solid nanofibers and a variety of CNTs, consistent with SEM observations in Figure 11. Catalyst particles detached from the surface are also evident, indicative of surface breakup processes.

of the uncoated mesh (Figures 11 and 13) reveal the variety of structures catalyzed by the surface. A tremendous variation in CNT lengths, diameters, and curvatures are evident from the images. The variations in size, opacity, and contrast across radial dimensions (particularly between overlaid structures) suggest structures ranging from CNTs to solid nanofilaments. This distribution of CNT sizes and, in particular, the heterogeneity of structures is consistent with surface breakup processes producing catalyst particles.

These images stand in stark contrast to those observed in Figure 3 showing the results for the Co-coated catalyst using the same optimal ethylene flame conditions. In the Co system, the CNT density is higher and exhibits a much more uniform size distribution, reflecting the greater uniformity of the

deposited catalyst particles. This stands in stark contrast to the products of catalyst particles formed through a surface breakup process which is controlled by the random polycrystallinity of the unprocessed steel mesh. The higher magnification images (of Figure 3) illustrate a morphology consistent with CNTs and an absence of nanofibers or miscellaneous carbon structures. No odd or twisted shapes are found. Most importantly, no catalyst particles are observed at the tips or as fragments within the CNTs. This absence confirms that surface breakup processes are not contributing to CNT synthesis in this flame environment (C_2H_4 flame at $\phi = 1.62$). If this were the case, catalyst particles would be expected at some CNT tips, because, as observed previously and documented elsewhere,^{43–51} surface breakup will lead to both tip and base growth. Finally, the contrast variation observed for the Co-catalyzed CNTs in the SEM images suggests that nearly all the CNTs are graphitic MWNTs. This is confirmed by the TEM images of Figure 7.

It is instructive to compare the SEM images for the plain SS mesh treated in the C_2H_4 flame at $\phi = 1.62$ (Figure 11) with those for the Co-coated mesh (Figure 4c) treated with the C_2H_2 flame at $\phi = 1.62$. The catalyzed carbon structures from the Co-coated mesh, similar to those of the plain SS mesh from the ethylene flame (Figure 11), exhibit a wide variety of shapes ranging from CNTs to wormlike nanofibers. Notably, many of the catalyzed nanofilaments are highly kinked or coiled, which is indicative of a large catalyst particle where differential diffusion and precipitation rates cause inequities in the carbon supply to the nanofilament. As noted previously, the heterogeneity of structure, prevalence of particles at the CNT tips, and dependence upon the mesh polycrystallinity (mesh weave direction) tell the story of surface breakup generating the catalyst particles when no Co particles are deposited on the plain SS mesh. An even closer comparison can be made between the Co catalyst-coated SS mesh (Figure 4c) and a plain SS mesh treated with the same C_2H_2 flame at $\phi = 1.62$, shown in Figure 12. The high similarity of the structures confirms an absence of catalyst specificity in directing the CNT growth under these flame conditions.

Catalyst Comparison: TEM. These comparisons may be further illustrated by the detailed nanostructure of the catalyzed products. Differences between the catalyzed growths are further highlighted by TEM images shown in Figure 13 for the plain SS mesh produced in the ethylene flame at $\phi = 1.62$. Consistent with the SEM images, a variety of features ranging from CNTs to nanofibers and other ill-formed structures are observed. Furthermore, there is considerable variation in CNT diameters, which is consistent with their catalysis by a random variation in catalyst particle size as produced by surface breakup. These features stand in contrast to the uniformly sized CNTs and absence of other catalyzed structures in Figure 7. These CNTs mirror uniformly sized, supported catalyst particles for the Co-coated SS mesh treated with this C_2H_4 flame.

We also note from the low-magnification TEM image (Figure 13) that the relative CNT yield is low for the plain SS mesh. With catalyst formation proceeding through surface breakup, carbon growth will be preferentially catalyzed along grain boundaries and lattice dislocations, reflecting the weakest areas of the surface. Such features are determined by the polycrystallinity of the substrate, thereby accounting for the irregularity of the catalyzed structures. These differences between the catalyzed products using the Co catalyst-coated and uncoated SS meshes within the C_2H_4 flame confirm the dominance of the Co catalyst in directing the catalyzed growth within this flame system.

In agreement with the SEM results, the catalyzed products from the plain SS mesh (treated with the C_2H_4 flame at $\phi = 1.62$, Figure 13) appear to be similar to those using the Co catalyst-coated SS mesh treated with a C_2H_2 flame at $\phi = 1.62$ seen in Figure 10. Particles at tube tips, nanofilaments ranging from CNTs to nanofibers, and irregular structures appear in both cases. This suggests that surface breakup processes are heavily contributing to the catalyzed products for the acetylene flames, regardless of the Co catalyst coating.

This similarity is further observed for an uncoated SS mesh and the Co catalyst-coated SS mesh treated with the C_2H_2 flame at $\phi = 1.62$, as illustrated by the TEM images in Figures 14 and 10, respectively. The heightened similarity between the catalyzed products and their relative yield within the same flame environment dramatically illustrates the absence of catalyst influence in directing the CNT growth under these flame conditions.

Summary of Catalyst and Surface Roles. As illustrated in the SEM images in Figure 11 and TEM images in Figure 13 for the noncatalyst-coated SS mesh, the catalyzed products assume a much wider distribution of diameters and morphologies and types compared to the deposited Co catalyst meshes, as illustrated in Figures 3 and 7 for the C_2H_4 flame at $\phi = 1.62$. This contrast confirms the catalyst specificity for directing the CNT growth within the ethylene flame environment. Most significantly, catalyst particles are observed at many tips using the uncoated SS mesh, characteristic of surface breakup processes. In general, this surface breakup will produce larger catalyst particles than those initially deposited upon the substrate, as documented by numerous carbon filament formation studies.^{45–54} The amount of surface breakup may not necessarily increase with increasing CO concentration; higher CO concentrations will lead to coking and subsequent deactivation of the surface, thereby shutting down catalytic activity.⁵⁵

This surface breakup mechanism also accounts for the high similarity between the SEM and TEM images (Figures 4 and 10, respectively) for the Co catalyst-coated mesh treated with the C_2H_2 at $\phi = 1.62$ and those using the noncatalyst-coated SS mesh (Figures 12 and 14, respectively). In the former cases, the CO concentration is too high to allow only the deposited catalyst to govern CNT synthesis. Carbide formation followed by surface breakup occurs, yielding a myriad of catalyst particles of varying size and shape. Although the deposited catalyst particles participate, too, they may also be removed from the surface and will likely undergo fragmentation through similar processes. In the absence of a deposited catalyst, as for the uncoated SS mesh, only catalyst “particles” formed by surface breakup can result in CNT synthesis. A vast variety of catalyzed structures is then produced, as seen in the SEM and TEM images of the uncoated SS mesh (Figures 12 and 14, respectively). The higher CO concentrations and lower H_2 concentrations exacerbate these processes within the acetylene flame at $\phi = 1.62$.

In summary, the similarity in the catalyzed products from the acetylene flames catalyzed by the coated and noncoated SS meshes illustrates the dominant role of the metal substrate in contributing to nanofilaments and nanofiber growth. Correspondingly, the vast difference between the catalyzed products for the ethylene flame of $\phi = 1.62$ and those of the uncoated SS mesh confirms the dominant role of the deposited catalyst particles as governing the CNT size, morphology, and surface coverage within that flame environment.

Roles of Flame Gases. Flame gases determine carbide formation and catalytic site deactivation; for completeness, the

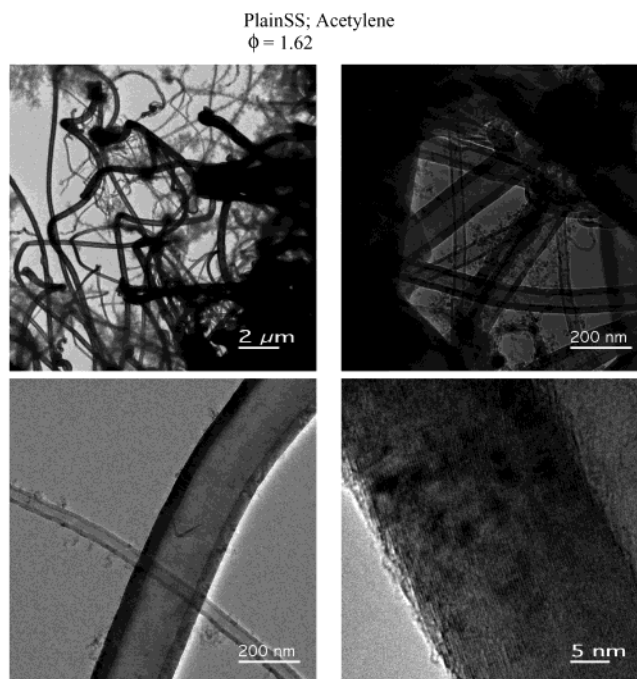


Figure 14. A series of TEM images for a plain (no catalyst deposit) SS mesh immersed within the flame gases produced by an acetylene flame at $\phi = 1.62$. Very large CNTs and solid nanofibers are produced, in high density, consistent with the SEM images of Figure 12.

role of the individual gases is briefly discussed here. Extended discussions may be found elsewhere.²⁵

CO and H_2 . As the carbon-bearing gas, CO serves as the carbon source for CNT synthesis. CO can contribute surface carbon through both the Boudouard and hydrogenation reactions. Each of these reactions likely contributes to carbon deposition upon the catalyst particle, prior works have found both processes competitive within the temperature range used here.⁴³

H_2 can influence metal-catalyzed CNT synthesis both chemically and physically. Coadsorbing H_2 will readily dissociate upon transition metals at elevated temperatures.⁵⁶ The resulting H-atoms can combine with elemental carbon and hydrocarbon fragments to fulfill valencies and thereby effect gasification.^{56–59} Thus, H_2 can act to etch or remove surface-adsorbed carbon. This surface cleaning process is particularly important where the rate of carbon deposition exceeds that of solvation, such as occurs at high gas-phase CO concentrations. Such buildup would facilitate carbide formation followed by surface breakup, creating a wide range of catalyst particle sizes and shapes.^{43–54}

This phenomenon accounts for the rich variety of structures catalyzed within the C_2H_2 flame at all equivalence ratios. Hence, the specificity of the deposited catalyst for directing the CNT synthesis is lost. The H_2 concentration plays a critical role in maintaining suitable CNT synthesis conditions. Evidence of this role is observed in comparing the SEM images for the C_2H_2 flame at $\phi = 1.62$ (Figure 4c) with those for the C_2H_4 flame at $\phi = 1.62$ (Figure 3b) and with the C_2H_6 flame at $\phi = 1.52$ (Figure 2a). With increasing CO mole fraction at a rather constant H_2 concentration, the CNT yield and graphitic quality initially increases and then decreases while undesirable, irregular nanofilaments become the dominant catalyzed product. Further comparisons supporting this vital role of H_2 relative to the CO mole fraction are observed by comparing the corresponding TEM images for these flames (Figures 10, 7, and 9, respectively).

The CO concentration is also key. At very high CO concentrations, surface carbon will build up to form an inactive layer upon the catalyst surface (coking layer) without a carbon removal mechanism. Once formed, such a layer prevents further contact with carbon gas-phase species and thus stops the carbon atom supply. This may account for the decline in relative yield of all catalyzed products using the C_2H_2 flame at $\phi = 1.62$. Catalyst deactivation by carbonaceous coverage is a well-known problem in the catalytic hydrogenation of unsaturated hydrocarbons.⁵⁵

Alternatively, H_2 can promote carbon deposition by electronic interactions with coadsorbates, particularly CO.^{56–60} This occurs by charge donation from dissociated H_2 to the CO antibonding $2\pi^*$ orbital thereby weakening the intramolecular bond while strengthening the metal-C bond. This enhancement, however, is not highly sensitive to the amount of H_2 present, beyond a few percent.⁵⁸

Physical effects of H_2 upon carbon deposition derived from dissociative adsorption include competitive adsorption^{57,59} and restructuring.⁶⁰ Both interactions are known to occur from bulk single-crystal studies.⁶⁰ High concentrations of H_2 could compete for adsorption sites on the catalyst surface, thereby slowing the rate of CO adsorption and subsequent carbon supply to the CNT. Significant coadsorbed levels of H_2 , through electronic interactions, could initiate restructuring of the catalyst particle surface. The elevated temperature within the flame environment, minimizing the activation energy required for such restructuring could synergistically interact with adsorbate-induced restructuring.²⁸

By comparison of the results for a constant CO concentration, we can gauge the relative contributions of these different roles. As seen in Table 1, the C_2H_6 flame with $\phi = 1.83$, the C_2H_4 flame with $\phi = 1.62$, and the C_2H_2 flame with $\phi = 1.43$ have identical CO concentrations but differ in the H_2 concentration by over 300%. Notably, the CO concentration chosen for this comparison is that which proved optimal for CNT yield and quality (Figures 3 and 7, SEM and TEM images, respectively) for the C_2H_4 flame.

Cross comparison of the SEM and TEM images for these flames provides the necessary data for assessing the roles of H_2 . As seen in Figure 4 for C_2H_2 at $\phi = 1.43$, the catalyzed growth consists mainly of irregularly shaped nanofibers and solid, nongraphitic filaments. Only a few CNTs are observed. Catalyst particles are also observed at some CNT tips, indicative of a surface breakup process. The corresponding TEM images (Figure 6) confirm the poor quality of the catalyzed structures with a lack of desirable graphitic CNTs. If removal of surface carbon was restricted at this low H_2 concentration, a high concentration of dissolved carbon could develop, leading to carbide formation, surface breakup, and random catalyst creation leading to the observed structures.^{43–54} Local deactivation of the catalytic surface by carbon fragments could further contribute to nonlinear growth by shunting the carbon source to other sites, thereby forcing morphological changes in the evolving carbon nanostructure to accommodate a spatially varying carbon supply.⁶¹ This surface breakup-catalysis mode is consistent with that discussed earlier for the series of flames where the H_2 concentration was maintained approximately constant.

Higher H_2 concentrations greatly facilitate the catalysis of uniform and graphitic CNTs. An absence of visible catalytic particles and their fragments along with the high density of uniform growth (SEM images, Figure 3; TEM images, Figure 7) confirms the specificity of the deposited Co catalyst toward the CNT catalysis using the ethylene flame with $\phi = 1.62$. These

results are consistent with H_2 both etching excess surface carbon and possibly reducing surface carbides back to elemental metal. This dramatic variation in product yield and quality at a constant CO concentration clearly illustrates the importance of both the H_2 and CO concentrations.

Yet higher H_2 concentrations, such as for ethane at $\phi = 1.83$, prove mildly poorer for CNT synthesis. Though CNTs are produced in abundance, as seen in the SEM images (Figure 2), their much larger size suggests that additional carbon is being supplied by the surface. Moreover, the presence of nanofibers and other structures absent in the ethylene flame are now apparent from the TEM images of Figure 8. These changes likely reflect a confluence of electronically enhanced dissociative adsorption and direct or thermally assisted surface restructuring. If the effective diameters of the catalyst particles increased with surface restructuring, this would then account for the large diameters of CNTs.

H_2O and CO_2 . H_2O and CO_2 both participate indirectly with CNT synthesis through the water-gas shift equilibria.³⁹ As the concentrations of these gases do not change dramatically within the CNT synthesis region, this participation is rather constant. Potential interference of these gases would include interaction with the catalyst particle and coadsorbates. CO_2 is not known to contribute to the surface reactions nor to interfere with adsorption of H_2 or CO. H_2O can interact with the adsorbed carbon upon the particle surface. Gasification of surface carbon by H_2O at elevated temperatures is well documented within catalysis literature.⁵⁵ Therein, water may play an essential role in maintaining a catalytically active particle surface. With oxidation removing deposited carbon, a slower rate of solvation and dissolution will result. This will affect the CNT growth rate, ultimate length, and graphitic structure, as discussed above. Future experiments will be directed to discern these effects.

Conclusions

The work presented here illustrates the possibilities of flame-synthesized growth of CNTs directly on a supporting substrate to be used in the final application. Direct growth precludes detrimental, time-intensive processing steps and thus has great commercial viability. We demonstrate this approach using catalysts deposited upon SS meshes.

Through choice of fuel based on C/H ratio and flame fuel/air equivalence ratio, a range of CO and H_2 post-flame concentrations were realized. Within the boundaries established by ethane and acetylene fuels, a region has been identified as conducive to CNT synthesis. Within this H_2 –CO concentration map, considerable variations in CNT yield and quality are observed. These variations are understood in terms of the interaction of the flame gases with the catalyst particles and the supporting substrate.

The base growth mechanism appears to dominate at low CO concentrations as very few catalyst particles are evident at CNT tips as observed in the SEM images for CO mole fractions less than 0.1. In contrast, the higher CO concentrations result in tip growth where deposited catalyst particles and surface fragments become detached from the surface through breakup induced by surface carbide formation. The former mechanism has better potential for synthesis of CNTs with uniform size and graphitic structure. With these criteria, using SEM and TEM imaging, CO and H_2 mole fractions near 0.105 proved optimal. Such conditions are realized by using a premixed ethylene–air mixture of $\phi = 1.62$. With the delineation of these reactive gas composition boundaries and an understanding of their origin, a path is set for scaling flame synthesis of CNTs using supported catalyst methods.

Acknowledgment. This work was supported by a NASA NRA 97-HEDs-01 combustion award (RVW) and through the NASA-Glenn Strategic Research Fund, each administered through NASA cooperative agreement NAC3-544 with The National Center for Microgravity Research on Fluids and Combustion (NCMR) at The NASA-Glenn Research Center. The authors gratefully acknowledge David R. Hull for the HRTEM imaging.

References and Notes

- (1) Dagani, R. *C&E News*, January 14, **2002**, pp 25–28.
- (2) Park, C.; Engel, E. S.; Crowe, A.; Gilbert, T. R.; Rodriguez, N. M. *Langmuir* **2000**, *16*, 8050.
- (3) Claye, A. S.; Fischer, J. E.; Huffman, C. B.; Rinzler, A. G.; Smalley, R. E. *J. Electrochem. Soc.* **2000**, *147*, 2845.
- (4) Maurin, G.; Bousquet, Ch.; Henn, F.; Bernier, P.; Almairac, R.; Simon, B. *Chem. Phys. Lett.* **1999**, *312*, 14.
- (5) Lu, W.; Chung, D. D. L. *Carbon* **2001**, *39*, 493.
- (6) Rodriguez, N. M. *J. Mater. Res.* **1993**, *8*, 3233.
- (7) Steigerwait, E. S.; Deluga, G. A.; Lukehart, C. M. *J. Phys. Chem. B* **2002**, *106*, 760.
- (8) Rodriguez, N. M.; Kim, M.-S.; Baker, R. T. K. *J. Phys. Chem.* **1994**, *98*, 13108.
- (9) Ajayan, P. M.; Stephan, O.; Colliex, C.; Trauth, D. *Science* **1994**, *265*, 1212.
- (10) Andrews, R.; Jacques, D.; Rao, A. M.; Rantell, T.; Derbyshire, F.; Chen, Y.; Chen, J.; Haddon, R. C. *Appl. Phys. Lett.* **1999**, *75*, 1329.
- (11) Schadler, L. S.; Giannaris, S. C.; Ajayan, P. M. *Appl. Phys. Lett.* **1998**, *73*, 3842.
- (12) Bower, C.; Rosen, R.; Jin, L.; Han, J.; Zhou, O. *Appl. Phys. Lett.* **1999**, *74*, 3317.
- (13) Alvarez, W. E.; Kitiyanan, B.; Borgna, A.; Resaco, D. E. *Carbon* **2001**, *39*, 547.
- (14) Su, M.; Zheng, B.; Liu, J. *Chem. Phys. Lett.* **2000**, *322*, 321.
- (15) Colomer, J.-F.; Stephan, C.; Lefrant, S.; Van Tendeloo, G.; Willems, I.; Konya, Z.; Fonseca, A.; Laurent, Ch.; Nagy, J. B. *Chem. Phys. Lett.* **2000**, *317*, 83.
- (16) Cassell, A. M.; Raymakers, J. A.; Kong, J.; Dai, H. J. *Phys. Chem. B* **1999**, *103*, 6484.
- (17) Andrews, R.; Jacques, D.; Rao, A. M.; Derbyshire, F.; Qian, D.; Fan, X.; Dickey, E. C.; Chen, J. *Chem. Phys. Lett.* **1999**, *303*, 467.
- (18) Cheng, H. M.; Li, F.; Su, G.; Pan, H. Y.; He, L. L.; Sun, X.; Dresselhaus, M. S. *Appl. Phys. Lett.* **1998**, *72*, 3282.
- (19) Hafner, J. H.; Bronikowski, M. J.; Azamian, B. R.; Nikolaev, P.; Rinzler, A. G.; Colbert, D. T.; Smith, K. A.; Smalley, R. E. *Chem. Phys. Lett.* **1998**, *296*, 195.
- (20) Cassell, A. M.; Raymakers, J. A.; Kong, J.; Dai, H. J. *Phys. Chem. B* **1999**, *103*, 6484.
- (21) Flahaut, E.; Govindaraj, A.; Peigney, A.; Laurent, Ch.; Rousset, A.; Rao, C. N. R. *Chem. Phys. Lett.* **1999**, *300*, 236.
- (22) Monthieux, M.; Smith, B. W.; Burteaux, B.; Claye, A.; Fischer, J. E.; Luzzi, D. E. *Carbon* **2001**, *39*, 1251.
- (23) Zhao, B.; Hu, H.; Niyogi, S.; Itkis, M. E.; Hamon, M. A.; Bhowmik, P.; Meier, M. S.; Haddon, R. C. *J. Am. Chem. Soc.* **2001**, *123*, 11673.
- (24) Chiang, I. W.; Brinson, B. E.; Smalley, R. E.; Margrave, J. L.; Hauge, R. H. *J. Phys. Chem B* **2001**, *105*, 1157.
- (25) Vander Wal, R. L., *Combust. Flame*, in press.
- (26) Vander Wal, R. L.; Hall, L. J. *Chem. Phys. Lett.* **2001**, *349*, 178.
- (27) Vander Wal, R. L.; Ticich, T. M. *Chem. Phys. Lett.* **2001**, *336*, 24.
- (28) Vander Wal, R. L.; Ticich, T. M. *J. Phys. Chem. B* **2001**, *105*, 10249.
- (29) Vander Wal, R. L.; Ticich, T. M.; Curtis, V. E. *Chem. Phys. Lett.* **2000**, *323*, 217.
- (30) Vander Wal, R. L.; Ticich, T. M.; Curtis, V. E. *J. Phys. Chem. A* **2000**, *104*, 7209.
- (31) Vander Wal, R. L.; Ticich, T. M.; Curtis, V. E. *J. Phys. Chem. B* **2000**, *104*, 11606.
- (32) Vander Wal, R. L.; Hall, L. J.; Berger, G. M. The 29th International Combustion Symposium, in press.
- (33) Vander Wal, R. L. *Chem. Phys. Lett.* **2000**, *324*, 217.
- (34) Yuan, L.; Saito, K.; Pan, C.; Williams, F. A.; Gordon, A. S. *Chem. Phys. Lett.* **2001**, *340*, 237.
- (35) Yuan, L.; Saito, K.; Hu, W.; Chen, Z. *Chem. Phys. Lett.* **2001**, *346*, 23.
- (36) Borman, G. L.; Ragland, K. W. *Combustion Engineering*; WCB McGraw Hill Inc.: New York, 1998.
- (37) *The Combustion Handbook*; Zink, J., Ed.; Wiley and Sons: New York, 2000.
- (38) Symth, K. C.; Miller, J. H.; Dorfman, R. C.; Mallard, W. G.; Santoro, R. J. *Combust. Flame* **1985**, *62*, 157.
- (39) Turns, S. R. *An introduction to combustion: Concepts and Applications*; McGraw-Hill Inc.: New York, 1996.
- (40) Rodriguez, N. M.; Chambers, A.; Baker, R. T. K. *Langmuir* **1995**, *11*, 3862.
- (41) Tibbets, G. G.; Devour, M. G.; Rodda, E. J. *Carbon* **1989**, *27*, 315.
- (42) Sinnott, S. B.; Andrews, R.; Qian, D.; Rao, A. M.; Mao, Z.; Dickey, E. C.; Derbyshire, F. *Chem. Phys. Lett.* **1999**, *315*, 25–30.
- (43) Geurts, F. W. H. A.; Sacco, A., Jr. *Carbon* **1992**, *30*, 415.
- (44) Jablonski, G. A.; Guerts, F. W.; Sacco, A., Jr. *Carbon* **1992**, *30*, 99.
- (45) Soneda, Y.; Makino, M. *Carbon* **2000**, *38*, 475.
- (46) Jablonski, G. A.; Geurts, F. W.; Sacco, A., Jr.; Biederman, R. R. *Carbon* **1992**, *30*, 87.
- (47) Sacco, A., Jr.; Geurts, F. W. H. A.; Jablonski, G. A.; Lee, S.; Gately, R. A. *J. Catal.* **1989**, *119*, 322.
- (48) Bradley, J. R.; Chen, Y.-L.; Sturmer, H. W. *Carbon* **1985**, *23*, 715.
- (49) Sacco, A., Jr.; Thacker, P.; Chang, T. N.; Chiang, A. T. S. *J. Catal.* **1984**, *85*, 224.
- (50) Guinot, J.; Audier, M.; Coulon, M.; Bonnetain, L. *Carbon* **1981**, *19*, 95.
- (51) Baird, T.; Fryer, J. R.; Grant, B. *Carbon* **1974**, *12*, 591.
- (52) Derbyshire, F. J.; Presland, A. E. B.; Trimm, D. L. *Carbon* **1975**, *13*, 111.
- (53) Presland, A. E. B.; Walker, P. L., Jr. *Carbon* **1969**, *7*, 1.
- (54) Ruston, W. R.; Warzee, M.; Hennaut, J.; Waty, J. *Carbon* **1969**, *7*, 47.
- (55) Bartholomew, C. H. *Catal. Rev. Sci. Eng.* **1982**, *24*, 67.
- (56) Somorjai, G. A.; Kim, C. M.; Knight, C. In *Surface science of catalysis: In situ probes and reaction kinetics*; (Dwyer, D. J., Hoffman, F. M., Eds.; American Chemical Society, Washington, DC, 1992).
- (57) Park, C.; Rodriguez, N. M.; Baker, R. T. K. *J. Catal.* **1997**, *169*, 212.
- (58) Nolan, P. E.; Lynch, D. C.; Cutler, A. H. *Carbon* **1994**, *32*, 477.
- (59) Yang, K. L.; Yang, R. T. *Carbon* **1986**, *24*, 687.
- (60) Campuzano, J. C. In *The chemical physics of solid surfaces and heterogeneous catalysis*; (King, D. A., Woodruff, D. P., Eds.; Elsevier: New York, 1990; Vol. 3, Chapter 4, pp 389–470).
- (61) Boellaard, E.; De Bokx, P. K.; Kock, A. J. H. M.; Geus, J. W. J. *Catal.* **1985**, *96*, 481.